



Analyses of acoustofluidic field in ultrasonic needle–liquid–substrate system for micro-/nanoscale material concentration

Qiang Tang¹ · Pengzhan Liu¹ · Junhui Hu¹

Received: 20 November 2017 / Accepted: 26 March 2018 / Published online: 4 April 2018
© Springer-Verlag GmbH Germany, part of Springer Nature 2018

Abstract

The ultrasonic needle–liquid–substrate system, in which an ultrasonically vibrating steel needle is inserted into an aqueous suspension film of micro-/nanoscale materials on a nonvibration silicon substrate, has large potential applications in micro-/nanoconcentration. However, research on its detailed concentration mechanism and the structural parameters' effect on concentration characteristics has been scarce. In this work, the acoustic streaming field and acoustic radiation force in an ultrasonic needle–liquid–substrate system, which are generated by a vibrating needle parallel to the substrate, are numerically investigated by the finite element method. The computational results show that the ultrasonic needle's vibration can generate the acoustic streaming field capable of concentrating micro-/nanoscale materials, and the acoustic radiation force has little contribution to the concentration. The computation results well explain the experimental phenomena that the micro-/nanoscale materials can be concentrated at some conditions and cannot at others. The computational results clarify the effects of the distance between the needle center and substrate surface, the needle's radius, the water film's height and radius and the shape of the needle's cross section on the acoustic streaming field and concentration capability.

Keywords Ultrasound · Vortex · Micro-/nanoscale material · Concentration · FEM

1 Introduction

Controlled concentration of micro-/nanoscale materials has huge potential applications in the self-assembling of micro-/nanomaterials (Wang and Lu 2012; Khoo et al. 2011; Liu et al. 2006; Zhou et al. 2006), fabrication of micro-/nanoelectronic components (Vincent and Destefanis 2013; Kulkarni and Zhong 2013), high-sensitivity sensing of biological substances (Buso et al. 1984), crystal growth (Kubota et al. 2000; Kuznetsov et al. 2001) and culture of artificial tissues (Minuth et al. 1998; Sittinger et al. 1997), etc. Among the physical methods for concentrating micro-/nanoscale materials, ultrasonic method for micro-/nanoscale material concentration has the merits such as very small temperature rise (<0.1 °C) and little heat damage to manipulated samples when the acoustic streaming is used to generate the manipulating force (Hu 2014), and little selectivity

to electromagnetic and optical properties of the samples (Bruus et al. 2011). In our previous work, we proposed and developed the ultrasonic needle–liquid–substrate system (Yang and Hu 2014; Tang et al. 2017b), which has been demonstrated to be capable of concentrating and repelling micro-/nanoscale materials. In the system, a stainless steel needle is inserted into the film of microscale suspension on a stationary substrate, and micro-/nanoscale materials near the ultrasonically vibrating needle and on the stationary substrate can be driven to the location under the needle and be concentrated. However, there has been little in-depth research on the details of concentration mechanism of the ultrasonic needle–liquid–substrate system before this work and on the structural parameters' effect on the concentration characteristics. The status quo is hindering the optimization design and applications of the ultrasonic needle–liquid–substrate system.

Owing to the limited performance of optical microscopes, the acoustic streaming fields observed in the experiments are usually incomplete (Tang and Hu 2015b; Liu and Hu 2017). Also, it is not easy to measure the acoustic radiation force acting on the individual micro-/nanoscale objects in the liquid film (Ding et al. 2012). Thus, it is quite inefficient

✉ Junhui Hu
ejhhu@nuaa.edu.cn

¹ State Key Lab of Mechanical and Control of Mechanical Structures, Nanjing University of Aeronautics and Astronautics, Nanjing 210016, China

and difficult to investigate the detailed mechanism of the ultrasonic needle–liquid–substrate system and the structural parameters' influences on the concentration characteristics by experimental methods. To obtain the in-depth and complete understanding of the concentration mechanism and the structural parameters' influences, theoretical computation of the acoustofluidic field is indispensable.

In this work, we analyze the acoustic streaming field and acoustic radiation force in the ultrasonic needle–liquid–substrate system by a finite element method (FEM) model. Based on the computation results, it is clarified that the micro-/nanoscale materials are concentrated by the microvortices of acoustic streaming rather than the acoustic radiation force. Our computational results also clarify the effects of the structural parameters such as the distance between the needle center and substrate surface, the needle's radius, the liquid film's height and radius and the shape of the needle's cross section on the acoustic streaming field and concentration capability.

2 Computational model and method

A math-physical model for the ultrasonic needle–liquid–substrate system is shown in Fig. 1, and its meshed FEM model is shown in Fig. 2. The mesh size of the acoustofluidic field near the ultrasonic needle is smaller than that in the rest region of the acoustofluidic field, in order to decrease the computational error of the acoustofluidic field near the needle, which is more important to the analyses and discussion in this work. In Fig. 1a, S1 and S2 are two cross sections of the water film, which are symmetric about and parallel to the needle and have a separation of one-third of the water film diameter. Unless otherwise specified, the detailed mesh sizes of different regions are as follows. Within the region of the liquid film between S1 and S2, the maximum element size is 0.18 mm (about 0.81% of the wavelength of the sound field in water at 67.8 kHz). In the rest region of the liquid film, the maximum element size is 0.34 mm (about 1.54% of the wavelength of the sound field in water at 67.8 kHz). Also, the maximum element size of the needle is 0.075 mm (about 21.4% of the needle's diameter). It was proved that the numerical results are mesh independent and convergent.

The detailed boundary conditions of the ultrasonic needle–liquid–substrate system for the sound field and acoustic streaming calculation in the liquid film are shown in Fig. 1. The computation of the acoustofluidic field is implemented by the FEM software COMSOL Multiphysics (version 4.3). In this work, only the steady-state acoustic streaming field is computed. The computational process consists of the following three steps (Tang and Hu 2015a, b; Tang et al. 2017a).

In the first step, the sound field is solved by the sound-structure coupling module with the boundary conditions

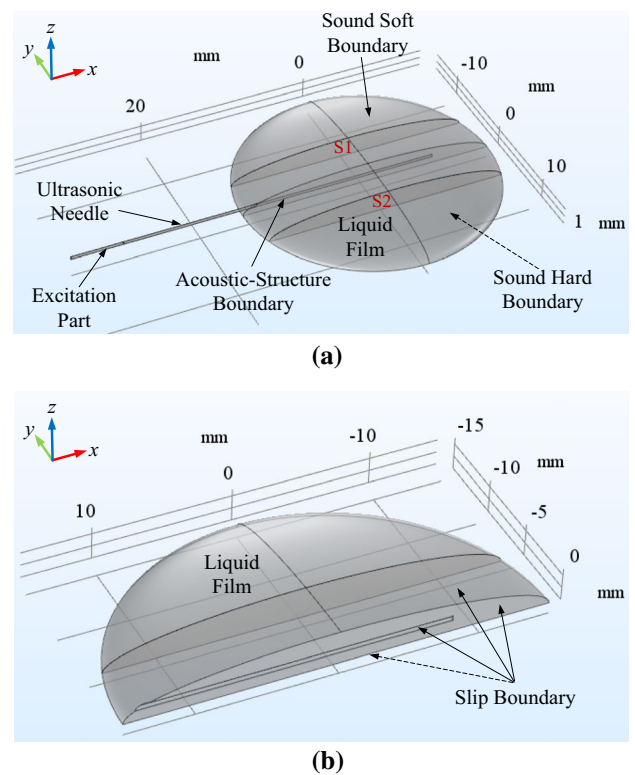


Fig. 1 (Color online) A 3D acoustofluidic field model for the ultrasonic needle–liquid–substrate system. **a** Boundary conditions for the sound field. **b** Boundary conditions for the acoustic streaming field

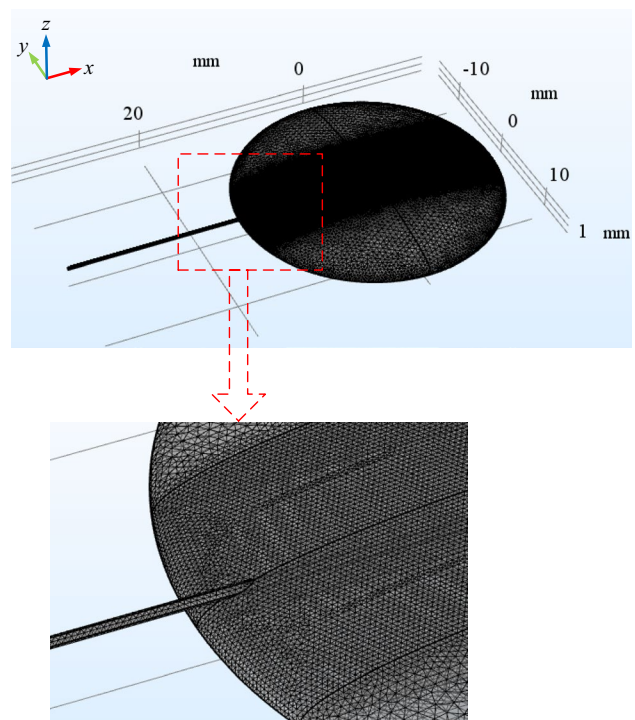


Fig. 2 (Color online) Meshed model for the acoustofluidic field

shown in Fig. 1a. Boundary conditions of the sound field are as follows: The normal acceleration is continuous at the interfaces between the ultrasonic needle and liquid film ($a_n^n = a_n^l$, where a_n^n represents the normal acceleration of the ultrasonic needle at the interfaces, and a_n^l represents the normal acceleration of the liquid film at the interfaces), which can be defined as acoustic-structure boundary; The interfaces between the liquid film and air are sound soft (sound pressure $p=0$) for the reason that ultrasound attenuates quickly in the air. The interface between the liquid film and substrate is sound hard ($\frac{\partial p}{\partial n} = 0$, where \mathbf{n} denotes the unit normal vector of the boundary). The following wave equation (Kinsler et al. 1999) is used to solve the sound field:

$$\rho_f \frac{\partial^2 p}{\partial t^2} = \rho_f c_f^2 \nabla^2 p + b \nabla^2 \frac{\partial p}{\partial t} \tag{1}$$

where p is the sound pressure, ρ_f is the fluid density without sound field, and c_f is the sound speed, and the acoustic dissipation factor b is computed by

$$b = \frac{4}{3} \eta + \eta' \tag{2}$$

where η and η' are the shear and bulk viscosity coefficient of the acoustic medium, respectively. The vibration velocity u_i (where subscript i represents x , y or z) of the sound field can be calculated according to (Hahn et al. 2015)

$$u_i = i \frac{1}{\rho_f \omega} \frac{\partial p}{\partial x_i} \tag{3}$$

where $i = \sqrt{-1}$ is the imaginary unit, and ω is the angular frequency.

In the second step, computed vibration velocity and sound pressure of the sound field are used to calculate the spatial gradient of the Reynolds stress and mean pressure (the second-order pressure in the sound field), by the postprocessing functions of the FEM software. The spatial gradients of the Reynolds stress and mean pressure are the force generating the acoustic streaming. The spatial gradient of the Reynolds stress F_j is computed by Lighthill (1978)

$$F_j = -\partial \langle \rho_f u_i u_j \rangle / \partial x_i \tag{4}$$

where u_i and u_j are the vibration velocities of the sound field, repeated suffix i and j represent x , y and z in the three-dimensional model, and $\langle \rangle$ represents the time average over one time period. The mean pressure \bar{p}_2 is computed by Tang and Hu (2015a)

$$\bar{p}_2 = \frac{1}{2 \rho_f c_f^2} \frac{B}{A} \langle p^2 \rangle \tag{5}$$

where $\frac{B}{A}$ is the nonlinear parameter of the medium (Beyer 1965, 1997).

In the last step, the steady acoustic streaming is solved by the fluidic dynamics module of the FEM software. Due to the symmetric characteristic of the acoustic streaming field produced by ultrasonically vibration in the y direction in our simulation model, only half of the liquid film is used to save the workstation's memory for the calculation, as shown in Fig. 1b. The steady acoustic streaming satisfies the following equation (Lighthill 1978; Hu 2014):

$$\rho_f (\bar{u}_i \partial \bar{u}_j / \partial x_i) = F_j - \partial \bar{p}_2 / \partial x_j + \eta \nabla^2 \bar{u}_j \tag{6}$$

where \bar{u}_i is acoustic streaming velocity. The acoustic streaming also satisfies the continuity equation

$$\partial \bar{u}_i / \partial x_i = 0 \tag{7}$$

Slip boundary condition ($\bar{u}_t \neq 0$ and $\bar{u}_n = 0$, which means that the tangential flow exists, while the normal flow velocity is zero) is used in the FEM computation of the acoustic streaming as shown in Fig. 1b. This is because our experiment shows that tangential acoustic streaming velocity can exist at the interfaces between the liquid film and substrate, the liquid film and needle and the liquid film and air (Yang and Hu 2014; Zhou et al. 2013). In the central plane (the xz plane), the flow velocity in the y direction is zero due to the symmetry, and thereby only the slip boundary condition is used.

3 Experimental verification

In order to experimentally verify the FEM simulation results, an ultrasonic needle–liquid–substrate system for the concentration of microparticles in a water film on a silicon substrate is constructed (Yang and Hu 2014). The experimental microscale particles (yeast cells) have an average diameter of 4–6 μm , and particle concentration in aqueous suspension is 0.048 mg/ml. Figure 3a shows a photograph of the experimental setup. Figure 3b shows the detailed size and structure of the ultrasonic needle–liquid–substrate system with a piezoelectric transducer to excite the vibration of the ultrasonic needle. The ultrasonic needle which is mechanically excited by the piezoelectric transducer is inserted into the aqueous suspension film on the substrate. In the piezoelectric transducer, four piezoelectric rings are aligned and pressed together by two cylindrical aluminum covers via a bolting structure. Its vibration direction and electrode configuration are also shown in Fig. 3b. The outer and inner diameters and the thickness of each piezoelectric ring in the transducer are 20, 6 and 1 mm, respectively. The electro-mechanical quality factor Q_m , piezoelectric coefficient d_{33} and relative dielectric constant $\epsilon_T^{33}/\epsilon_0$ of the piezoelectric ring are 2000, 325×10^{-12} m/V and 1450, respectively. Each cylindrical aluminum cover at the two ends of transducer

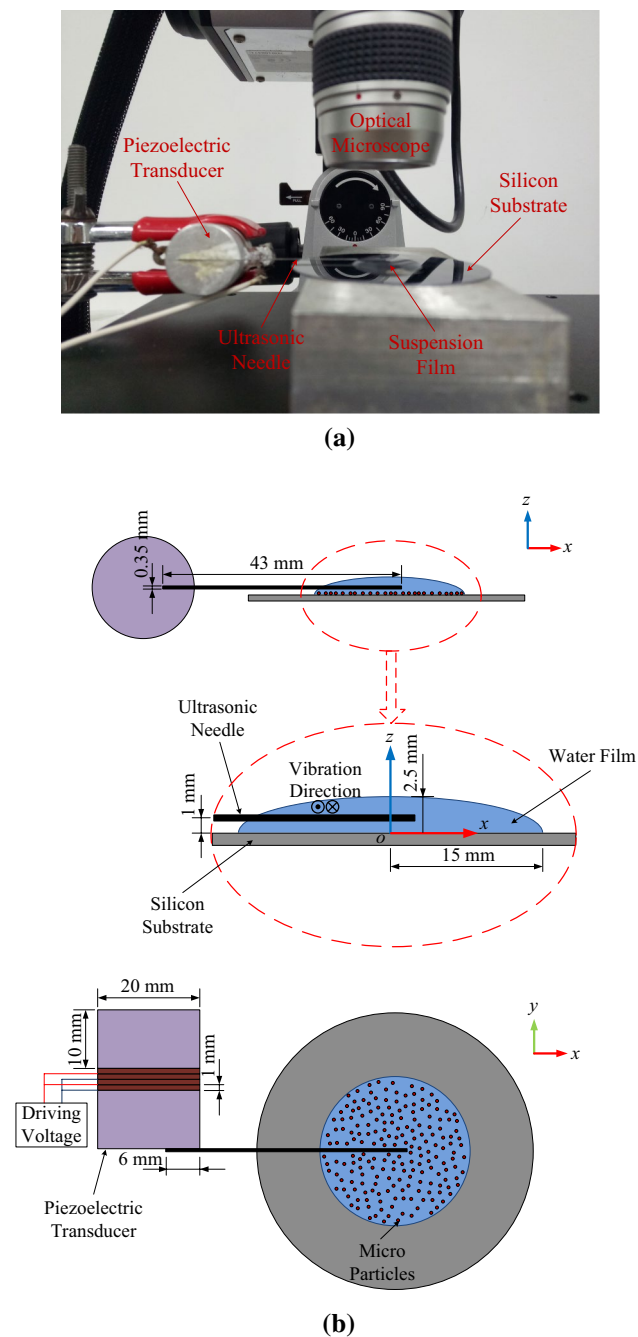


Fig. 3 (Color online) Experimental setup and the device to verify calculation results. **a** Photograph of the experimental setup. **b** Device structure and size

has a diameter of 20 mm and thickness of 10 mm. The steel needle is 43 mm long and 0.35 mm in diameter. The length of the needle bonded onto the piezoelectric transducer is 6 mm. The length of the needle inserted in the water film is about 22 mm. The distance between the ultrasonic needle center and substrate surface is controlled by an XYZ stage and is 1 mm in Fig. 3b. The maximum height and radius of the water film are 2.5 and 15 mm, respectively. The driving

voltage is sinusoidal, and the transducer works at resonance frequency of the needle (67.8 kHz). In Fig. 3b, the needle is excited by the transducer in the y direction. Thus, its vibration is parallel to the substrate. In the simulation, the center of the interface between the water film and substrate is defined as the origin o of the xyz coordinate system.

4 Results and discussion

To simplify the computation, the piezoelectric transducer used to excite the needle's vibration is not included in the FEM model. Also, unless otherwise specified, property parameters of the needle, liquid film (water) and micro-particles (yeast cells) shown in Table 1 (Liebermann 1949; Hawkes et al. 1997) are used.

To explain the experimental phenomena of microparticle concentration, the acoustic streaming field around the ultrasonic needle is computed, and flow patterns on the substrate are shown in Fig. 4a. In Fig. 4a, the color denotes the magnitude of the acoustic streaming velocity, and the arrow denotes the direction and magnitude of the acoustic streaming velocity. It is seen that there are some small regions near the needle (regions A–F), in which the flow velocity is much larger than that in the region farther away from needle. From Fig. 4a, it is seen that flow near the needle can drive the particles on the substrate to the location under the needle, and the symmetry of the flow on the two sides of the needle makes the particle concentration under the needle feasible. Figure 4b is the measured concentration pattern which was obtained by the yeast cells (Yang and Hu 2014). Comparing Fig. 4a, b, it is known that regions A–F in Fig. 4a correspond to lobed concentration spots A–F in Fig. 4b, respectively, and the distance between the neighboring locations of maximum inward flow velocity in Fig. 4a ($= 3$ mm) is very close to that between the neighboring locations of maximum width of the lobed concentration in Fig. 4b ($= 2.9$ mm). The average length L of concentration spots in the experiment is about 1.5 mm, while the average length of red regions in Fig. 4a, in which there is inward flow, is about 1.8 mm. The difference is because it is difficult to drive the particles on the substrate at the locations where the flow velocity is small.

Figure 4c shows the distribution of the y -directional acoustic streaming velocity. It is seen that there are inward and outward flows (for the needle) on the substrate. Dashed circles b1–b8 and r1–r7 are shown in Fig. 4c to indicate the regions of inward and outward flows, respectively. A ratio of the average of maximum inward flow velocities ($|v|_{\max,i}^{\text{in}}$ in the blue regions b1–b8) to the average of maximum outward flow velocities ($|v|_{\max,j}^{\text{out}}$ in the red regions r1–r7) is defined to quantify the concentration capability. The concentration ability γ is

Table 1 Parameters of the ultrasonic needle–liquid–substrate system

The water film’s height H_w (mm)	The water film’s radius R_w (mm)	The needle’s total length L_{nt} (mm)
2.5	15	43
The needle’s radius R_n (mm)	The distance between needle center and substrate surface D_{ns} (mm)	The excitation part length of needle L_{ne} (mm)
0.175	1	6
Density of water ρ_f (kg/m ³)	Sound speed in water c_f (m/s)	Shear viscosity of water η (Pa·s)
998	1479	0.001
Volume-to-shear viscosity ratio in water η'/η	Nonlinear parameter of water at room temperature B/A	Density of needle ρ_n (kg/m ³)
2.1	5	7850
Young’s modulus of needle E_n (Pa)	Poisson’s ratio of needle γ_n	Density of yeast cell ρ_p (kg/m ³)
2.05×10^{11}	0.28	1114
Sound speed in yeast cell c_p (m/s)	Average radius of yeast cell R_p (μ m)	Excitation amplitude of needle A_n (nm)
1606	3	150

$$\gamma = \frac{\frac{1}{M} \sum_{i=1}^M |v|_{\max,i}^{\text{in}}}{\frac{1}{N} \sum_{j=1}^N |v|_{\max,j}^{\text{out}}} \tag{8}$$

where M and N represent the total numbers of inward flow and outward flow regions, respectively.

For micromanipulation, there is always a question about which force is dominant during the manipulation process, the drag force induced by the acoustic streaming or acoustic radiation force applied on individual manipulated micro-objects (Muller et al. 2012; Barnkob et al. 2012). We calculated the y -directional starting drag force on a 6- μ m-diameter yeast cell at the interface between the water and substrate, which is caused by the y -directional acoustic streaming, and the result is shown in Fig. 5a. For comparison, we also calculated the y -directional acoustic radiation force on a 6- μ m-diameter yeast cell at the interface between the water and substrate, and the result is shown in Fig. 5b.

The y -directional starting drag force F_y^{drag} generated by the acoustic streaming is calculated by Surhone et al. (2010) and Hu (2014)

$$F_y^{\text{drag}} = 6\pi\eta R_p (\bar{u}_y - v_{py}) \tag{9}$$

where R_p is the average radius of manipulated particles (yeast cells), and v_{py} is the particle velocity in the y direction and set to be zero for the calculation of the starting drag force. The y -directional acoustic radiation force is calculated by Gor’Kov (1962), Hasegawa et al. (1988), Hasegawa and Yosioka (2005) and Hu (2014)

$$F_y^{\text{rad}} = -\frac{4}{3}\pi R_p^3 \frac{\partial}{\partial y} \left[\frac{1-\beta}{2\rho_f c_f^2} \langle p^2 \rangle - \frac{D}{2} \rho_f \langle u_x^2 + u_y^2 \rangle \right] \tag{10}$$

where parameters β and D can be expressed as

$$\beta = \frac{\rho_f c_f^2}{\rho_p c_p^2} \tag{11}$$

and

$$D = \frac{3(\rho_p - \rho_f)}{2\rho_p + \rho_f} \tag{12}$$

where ρ_p and c_p are the density and sound speed of the microparticles (yeast cells), respectively. The detailed parameter values of the yeast cells and acoustic medium (water) are listed in Table 1. According to the calculation results, it is known that the starting drag force generated by the acoustic streaming is larger than the acoustic radiation force by 10^5 times. That is the reason why the acoustic streaming is dominant in our micro-/nanoscale material concentration by the ultrasonic needle–liquid–substrate system (Yang and Hu 2014; Tang et al. 2017b).

The effects of the distance between the needle center and substrate surface D_{ns} on the concentration capability γ for different needle radii are computed at 67.8 kHz, and the result is shown in Fig. 6. In the calculation, the water film’s radius and height are kept constant (15 and 2.5 mm, respectively). The concentration capability increases first and then decreases as the distance between the needle center and substrate surface increases. Our previous experiments (Yang and Hu 2014) show that there exists a range of the distance between the needle center and substrate surface (from 0.5 to 2 mm), beyond which no particle concentration can be observed. The results in Fig. 6 clearly indicate that the concentration capability γ is less than 1 when the distance is beyond this range, which means that the averaged

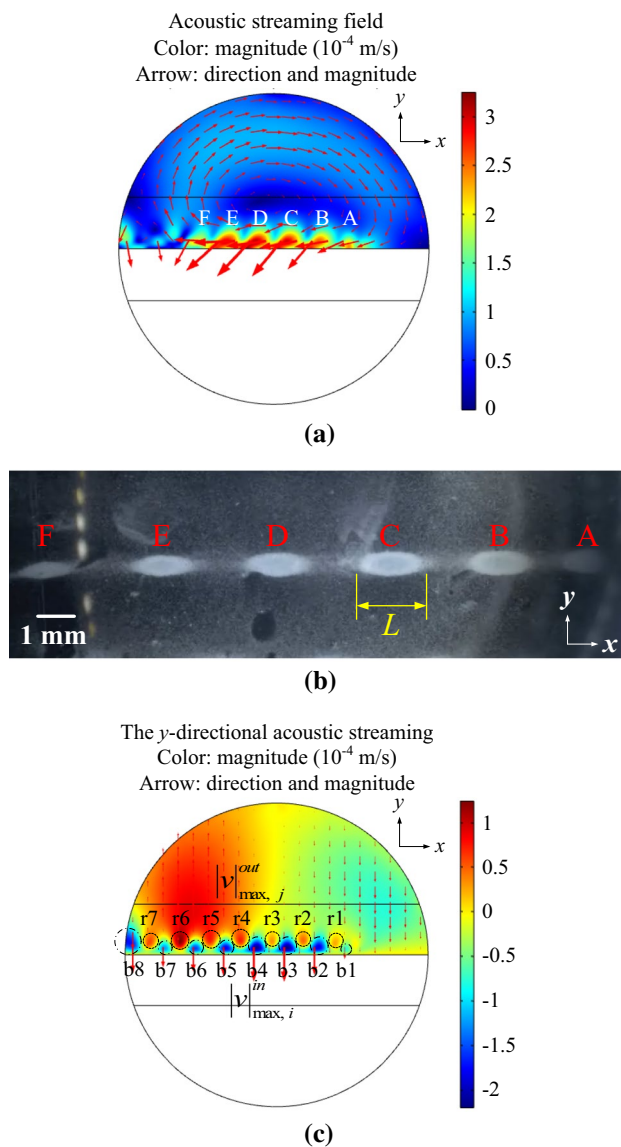


Fig. 4 (Color online) Acoustic streaming field on the substrate surface at 67.8 kHz and a photograph of the concentration pattern. **a** Calculated acoustic streaming field on the substrate. **b** Observed concentration pattern. **c** Distribution of the y-directional acoustic streaming velocity

inward flow velocity is smaller than the averaged outward flow velocity.

The measured and calculated minimum distances for the generation of the concentration effect at different needle radii in the experiments and calculated results are shown in Table 2. It is seen that there is a good agreement between the computed and measured results, and the larger the needle radius is, the larger the minimum distance is. For a given distance between the needle center and substrate, the distance between the needle and substrate decreases as the needle radius increases. This causes an increase in inward flow resistance and a decrease in outward flow resistance,

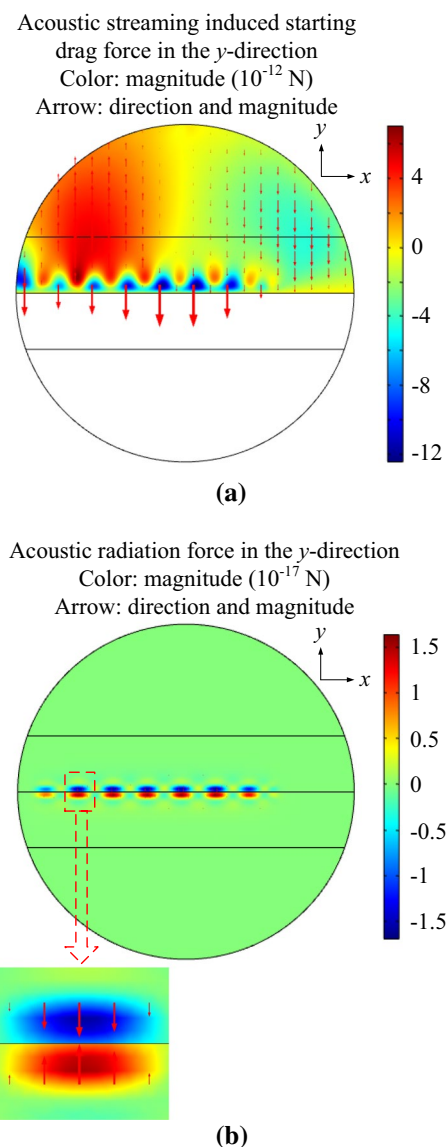


Fig. 5 (Color online) **a** Distribution of the y-directional acoustic streaming-induced starting drag force on the yeast cell on the substrate. **b** Distribution of the y-directional acoustic radiation force on the yeast cell on the substrate

which lowers the concentration capability. To maintain the concentration capability, one needs to raise the needle.

The dependency of the concentration capability γ on the water film's height and radius was computed at 68.7 kHz, and the results are shown in Fig. 7. Figure 7a shows that the concentration capability γ keeps almost constant for different water film height (from 1 to 4.5 mm). Figure 7b shows that the concentration capability γ keeps almost constant for different water film radius (from 10 to 20 mm). Thus, the water film's height and radius have little effect on the concentration capability γ , which are also in agreement with the experimental phenomena (Yang and Hu 2014; Tang

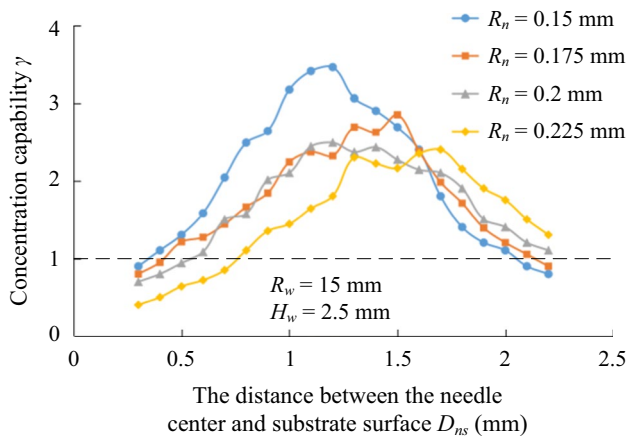


Fig. 6 (Color online) Effect of the distance between the needle center and substrate surface on the concentration capability for different needle radii at 67.8 kHz

Table 2 Measured and calculated minimum distances for the concentration at different needle radii

The needle’s radius R_n (mm)	0.15	0.175	0.2	0.225
Measured minimum distance (mm)	0.3	0.5	0.7	0.8
Calculated minimum distance (mm)	0.4	0.5	0.6	0.8

et al. 2017b). The water film’s size only affects the acoustic streaming field farther away from the needle and has little effect on the acoustic field and acoustic streaming near the needle. The nonsensibility of the concentration capability to the water film’s size is beneficial for lowering the requirement on the dispenser’s performance in repeatability.

The effects of the needle’s cross-sectional shape and size on the concentration capability were also calculated by the FEM. Elliptical, rectangular and rhombic cross sections of the needle were investigated. The calculation conditions are as follows: The working frequency and excitation amplitude of the needle are 67.8 kHz and 150 nm, respectively; the water film’s radius and height are 15 and 2.5 mm, respectively; the distance between the needle center and substrate surface is 1 mm. The maximum element size of the needle in the computation is kept to be about 20% of the needle’s minimum structural dimension when the needle’s cross-sectional shape and size change.

Figure 8 shows the calculated concentration capability versus half of the length of the axis a_n parallel to the substrate when the cross section is elliptical. In the computation, the ellipse area is kept constant ($S_n = \pi \times 0.175^2 \text{ mm}^2 \approx 0.0962 \text{ mm}^2$) and a_n changes from 0.075 to 0.275 mm. Figure 8a shows the FEM model viewed from the x direction. Figure 8b shows that as a_n increases, the concentration capability increases first and then changes little. Figure 8b also includes the calculation result for the needle with a circular

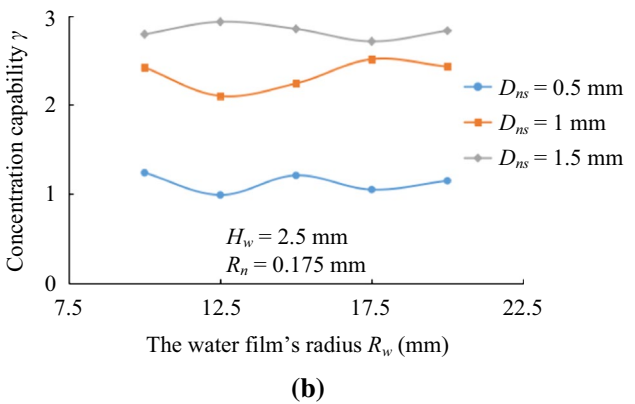
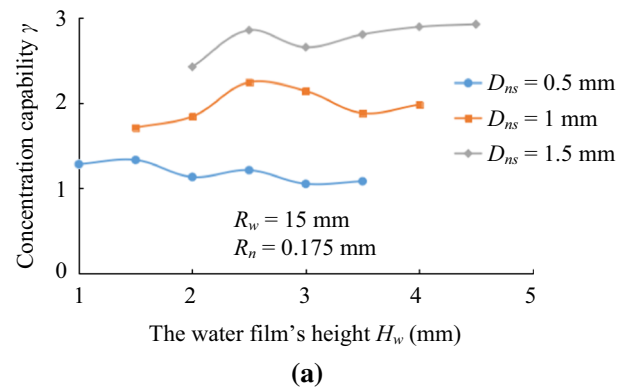


Fig. 7 (Color online) **a** Concentration capability versus the water film’s height. **b** Concentration capability versus the water film’s radius

cross section. It is known that the concentration capability may be improved if the commonly used needle with a circular cross section is vertically flattened along the z direction. For the elliptical cross section with a constant area, as a_n increases, the curvature of the needle’s surface facing the substrate decreases, which lowers the needle resistance to the inward flow. When a_n is large enough, the needle’s shape is close to a thin plate parallel to the substrate. In this case, the thickness change of the needle little affects the flow resistance.

Figure 9 shows the calculated concentration capability versus the side length L_n parallel to the substrate when the cross section is rectangular. In the computation, the rectangle area is kept constant ($S_n = 0.35^2 \text{ mm}^2 = 0.1225 \text{ mm}^2$) and L_n changes from 0.15 to 0.55 mm. Figure 9a shows the FEM model viewed from the x direction. It is seen that as L_n increases, the concentration capability decreases first and then changes little. Figure 9b also includes the calculation result for the needle with a square cross section. It is known that the concentration capability may be improved if the needle with a rectangular cross section is horizontally flattened along the y direction. Figure 10 shows the calculated concentration capability versus the diagonal length

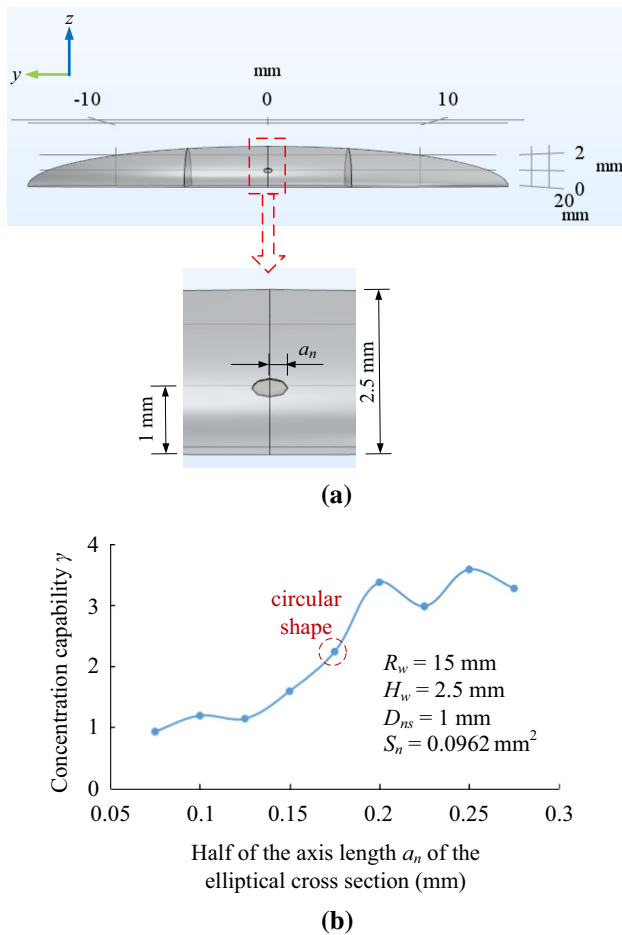


Fig. 8 (Color online) Calculated concentration capability versus half of the length of the axis a_n parallel to the substrate when the cross section is elliptical. **a** The FEM model viewed from the x direction. **b** Concentration capability at 67.8 kHz

L_{nd} parallel to the substrate when the cross section is rhombic. In the computation, the rhombus area is kept constant ($S_n = 0.1225$ mm²) and L_{nd} changes from 0.21 to 0.77 mm. Figure 10a shows the FEM model viewed from the x direction, and the rhombic angle facing the substrate is defined as θ . Figure 10b shows that as L_{nd} increases, the concentration capability increases first and then decreases. It is known that the maximum concentration capability may be achieved when the angle θ is about 36°. (The diagonal length of the rhombus is 0.28 mm.) The phenomena shown in Figs. 9 and 10 are explained as follows.

The sharp edge on a vibrating needle can generate strong local eddies due to very large spatial gradient of the Reynolds stress nearby (Hu et al. 2011; Hu 2014). When the needle in our experiments vibrates in the direction parallel to the substrate, the local eddies usually flow outward to the right or left side of the needle and flow back along the substrate surface, and generate the inward flow on the substrate, which positively contributes to the concentration capability.

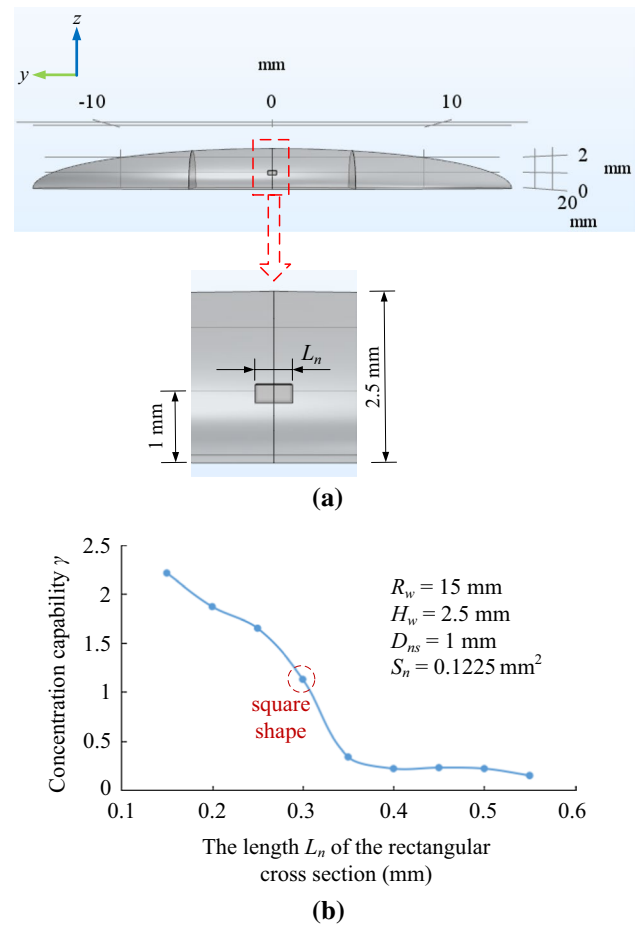


Fig. 9 (Color online) Calculated concentration capability versus the side length L_n parallel to the substrate when the cross section is rectangular. **a** The FEM model viewed from the x direction. **b** Concentration capability at 67.8 kHz

The rectangular cross section has right-angle edges, which generate the local eddies and positively contribute to the concentration capability. For the cross section with a constant area, as L_n increases, the distance between the needle's lower surface (facing the substrate) and the substrate increases, which decreases the edge caused inward flow on the substrate and lowers the concentration capability. When L_n is large enough, the distance between the needle's lower surface (facing the substrate) and the substrate is so large that the edge caused inward flow on the substrate affects little on the concentration capability. In this case, the concentration capability changes little with L_n . When the cross section of the needle is rhombic, the two side vertices can also generate the local eddies, which positively contribute to the concentration capability. For the cross section with a constant area, as L_{nd} increases, the distance between the lower vertex and substrate surface increases. This lowers the inward flow on the substrate and causes the decrease in the concentration capability.

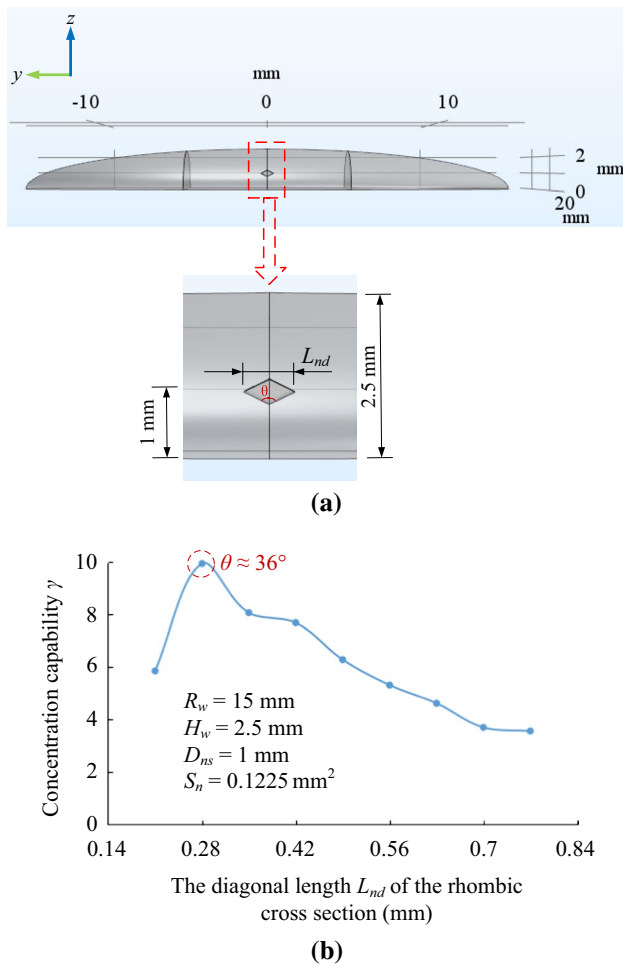


Fig. 10 (Color online) Calculated concentration capability versus the diagonal length L_{nd} parallel to the substrate when the cross section is rhombic. **a** The FEM model viewed from the x direction. **b** Concentration capability at 67.8 kHz

By the comparison of Figs. 8, 9 and 10, it is known that the concentration capability of the needle with a rhombic cross section is the highest and that of the needle with an elliptical one is the weakest when the lateral dimensions ($2a_n$, L_n and L_{nd}) are smaller. This phenomenon can also be well explained by the local eddies which are generated by the edges of the needle in vibration. The needle with a rhombic cross section has two sharp edges on its two sides. Also, compared with the rectangular cross section, it has smaller flow resistance to the inward flow due to its declining lower

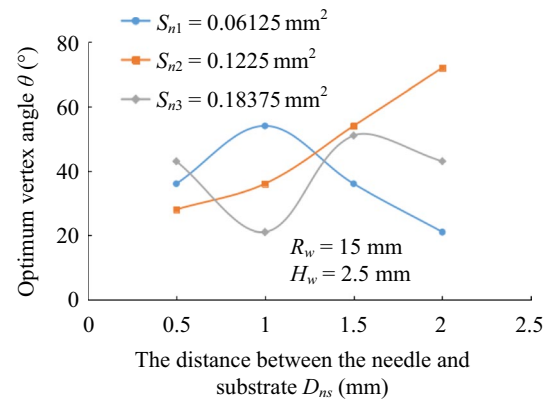


Fig. 11 (Color online) The dependence of the optimum vertex angle θ on the cross-sectional area of the needle and the distance between the needle center and substrate

surface. Thus, it has the strongest concentration capability at the smaller lateral dimension. The needle with an elliptical cross section has no sharp edge on its surface. Thus, it has the weakest concentration capability at the smaller lateral dimension.

Also by the comparison of Figs. 8, 9 and 10, it is also known that the concentration capability of the needle with a rectangular cross section is much smaller than those of the needle with the elliptical and rhombic ones when the lateral dimensions ($2a_n$, L_n and L_{nd}) are sufficiently large. This phenomenon is explained as follows. For the needle with a rectangular cross section, the thickness of the ultrasonic field between the needle and substrate is uniform, which makes its ultrasonic field on the substrate relatively uniform compared to the ones generated by the needles with the elliptical and rhombic cross sections. A uniform ultrasonic field on the substrate makes the spatial gradient of the Reynolds stress along the substrate very weak, which results in a very weak acoustic streaming along the substrate and very weak concentration stability. For the needle with an elliptical or rhombic cross section, the ultrasonic field between the needle and substrate has a larger thickness at the field's edge than at the center, which causes the acoustic streaming on the substrate to flow inward and relatively strong concentration stability.

Further FEM calculation indicates that the optimum vertex angle θ is affected by the distance between the needle center and substrate surface D_{ns} and the cross-sectional area of the needle S_n , as shown in Fig. 11. It shows that for

Table 3 Effects of the dimensions on the concentration capability at 67.8 kHz

	The distance between the needle center and substrate surface D_{ns}	The needle's radius R_n	The water film's height H_w	The water film's radius R_w	The shape of the needle's cross section
Concentration capability γ	Sensitive	Sensitive	Insensitive	Insensitive	Sensitive

a needle with the rhombic cross section of given size and shape, one may change the distance between the needle and substrate to achieve the optimal concentration effect.

From Figs. 8, 9, 10 and 11, it is seen that the concentration capability is affected by the shape and size of the cross section of the needle. The effects of the distance between the needle center and substrate surface, the needle's radius, the water film's height and radius and the shape of the needle's cross section on the concentration capability are summarized in Table 3.

In addition, a comparison of the streaming fields in the yz plane of an anti-nodal position along the needles with the elliptical ($a_n=0.075$ mm, $S_n=0.0962$ mm²), rectangular ($L_n=0.15$ mm, $S_n=0.1225$ mm²) and rhombic ($L_{nd}=0.28$ mm, $S_n=0.1225$ mm²) cross sections is listed in Fig. 12. It is confirmed that the sharp edges on the needles with the rectangular and rhombic cross sections can generate remarkable local eddies, while the needle with the elliptical cross section generates no local eddy as the needle surface is smooth.

5 Summary

We have numerically calculated and analyzed the acousto-fluidic field in the ultrasonic needle–liquid–substrate system. The FEM calculation results of the acoustic streaming field on the substrate can well explain the concentration pattern and size of microparticles in the experiment. By comparing the magnitudes of the acoustic streaming-induced drag force and the acoustic radiation force on the microparticles, it is clarified that the acoustic streaming has a dominant effect on the micro-/nanoscale material concentration. The calculation results also clarify the effects of the distance between the needle center and substrate surface, the needle's radius, the water film's height and radius and the shape of the needle's cross section on the concentration capability. The calculation results show that the concentration capability is insensitive to the water film's size, which lowers the requirement on the dispenser's performance in repeatability. Also, the distance between the needle and substrate, and the needle's shape and size have remarkable influence on the concentration capability of the acoustic streaming field on the substrate, which provides promising micro-/nanomanipulation methods to design the system. The ultrasonic needle–liquid–substrate system has the merits such as very small temperature rise (<0.1 °C), no heat damage to manipulated samples and little selectivity to electromagnetic and optical properties of the samples. It can be applied in the fabrication of nanosensors and other nanodevices, crystal growth, culture of artificial tissues, nanoassembling, etc.

Acknowledgements This work is supported by the following funding organizations in China: National Basic Research Program of China (973 Program, Grant No. 2015CB057501), National Natural Science

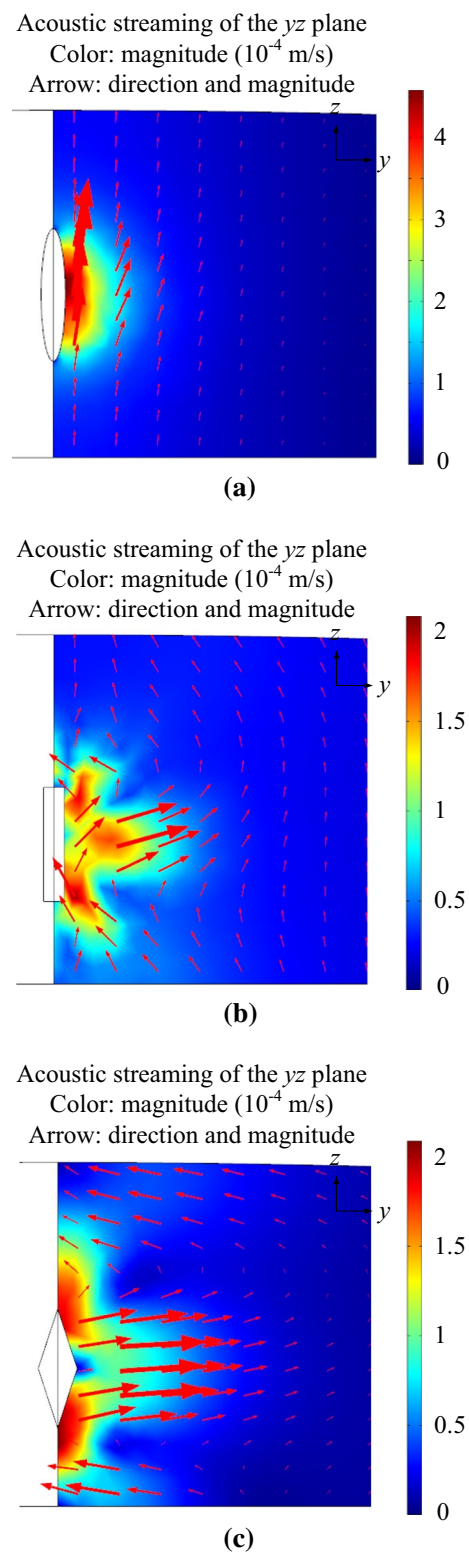


Fig. 12 (Color online) A comparison of the acoustic streaming fields in the yz plane for the needles with different cross sections. **a** Elliptical ($a_n=0.075$ mm, $S_n=0.0962$ mm²). **b** Rectangular ($L_n=0.15$ mm, $S_n=0.1225$ mm²). **c** Rhombic ($L_{nd}=0.28$ mm, $S_n=0.1225$ mm²)

Foundation of China (Grant 51505222), State Key Lab of Mechanics and Control of Mechanical Structures (Grant No. MCMS-0318K01), Postgraduate Research and Practice Innovation Program of Jiangsu Province (No. KYCX17_0237) and the Fundamental Research Funds for the Central Universities.

References

- Barnkob R, Augustsson P, Laurell T, Bruus H (2012) Acoustic radiation- and streaming-induced microparticle velocities determined by microparticle image velocimetry in an ultrasound symmetry plane. *Phys Rev E Stat Nonlinear Soft Matter Phys* 86(5 Pt 2):056307
- Beyer RT (1965) Nonlinear acoustics. In: Mason WP (ed) *Physical acoustics*, vol 2B. Academic Press, New York, pp 231–263
- Beyer RT (1997) The parameter B/A. In: Hamilton MF, Blackstock DT (eds) *Nonlinear acoustics: theory and applications*. Academic Press, New York, pp 25–39
- Bruus H, Dual J, Hawkes J, Hill M, Laurell T, Nilsson J, Radel S, Sadhal S, Wiklund M (2011) Forthcoming Lab on a Chip tutorial series on acoustofluidics: acoustofluidics-exploiting ultrasonic standing wave forces and acoustic streaming in microfluidic systems for cell and particle manipulation. *Lab Chip* 11(21):3579–3580
- Buso OP, Colautti P, Moschini G, Hu X, Stievano BM (1984) High sensitivity PIXE determination of selenium in biological samples using a preconcentration technique. *Nucl Instrum Methods B* 3(1–3):177–180
- Ding X, Lin SS, Kiraly B, Yue H, Li S, Chiang IK, Shi J, Benkovic SJ, Huang TJ (2012) On-chip manipulation of single microparticles, cells, and organisms using surface acoustic waves. *Proc Natl Acad Sci USA* 109(28):11105–11109
- Gor'kov LP (1962) On the forces acting on a small particle in an acoustical field in an ideal fluid. *Sov Phys Dokl* 6(1):773
- Hahn P, Leibacher I, Baasch T, Dual J (2015) Numerical simulation of acoustofluidic manipulation by radiation forces and acoustic streaming for complex particle. *Lab Chip* 15(22):4302–4313
- Hasegawa T, Yosioka K (2005) Acoustic-radiation force on a solid elastic sphere. *J Acoust Soc Am* 69(4):937–942
- Hasegawa T, Saka K, Inoue N, Matsuzawa K (1988) Acoustic radiation force experienced by a solid cylinder in a plane progressive sound field. *J Acoust Soc Am* 83(5):1770–1775
- Hawkes JJ, Limaye MS, Coakley WT (1997) Filtration of bacteria and yeast by ultrasound-enhanced sedimentation. *J Appl Microbiol* 82(1):39–47
- Hu J (2014) *Ultrasonic micro/nano manipulations: principles and examples*. World Scientific Publishing, Singapore
- Hu J, Zhu H, Li N, Zhao C (2011) Sound induced lobed pattern in aqueous suspension film of micro particles. *Sens Actuat A Phys* 167(1):77–83
- Khoo HS, Lin C, Huang SH, Tseng FG (2011) Self-assembly in micro- and nanofluidic devices: a review of recent efforts. *Micromachines* 2(1):17–48
- Kinsler LE, Frey AR, Coppens AB, Sanders JV (1999) *Fundamentals of acoustics*. Hamilton Press, Te Rapa
- Kubota N, Yokota M, Mullin JW (2000) The combined influence of supersaturation and impurity concentration on crystal growth. *J Cryst Growth* 212(3–4):480–488
- Kulkarni GS, Zhong Z (2013) Fabrication of carbon nanotube high-frequency nanoelectronic biosensor for sensing in high ionic strength solutions. *J Vis Exp* 77:e50438
- Kuznetsov YG, Malkin AJ, McPherson A (2001) The influence of precipitant concentration on macromolecular crystal growth mechanisms. *J Cryst Growth* 232(1–4):114–118
- Liebermann LN (1949) The second viscosity of liquids. *Phys Rev* 75:1415–1422
- Lighthill J (1978) Acoustic streaming. *J Sound Vib* 61(3):391–418
- Liu P, Hu J (2017) Controlled removal of micro/nanoscale particles in submillimeter-diameter area on a substrate. *Rev Sci Instrum* 88(10):105003
- Liu H, Zhai J, Jiang L (2006) The research progress in self-assembly of nano-materials. *Chin J Inorg Chem* 22(4):585–597
- Minuth WW, Sittinger M, Kloth S (1998) Tissue engineering: generation of differentiated artificial tissues for biomedical applications. *Cell Tissue Res* 291(1):1–11
- Muller PB, Barnkob R, Jensen MJ, Bruus H (2012) A numerical study of microparticle acoustophoresis driven by acoustic radiation forces and streaming-induced drag forces. *Lab Chip* 12(22):4617–4627
- Sittinger M, Schultz O, Keyszer G, Minuth WW, Burmester GR (1997) Artificial tissues in perfusion culture. *Int J Artif Organs* 20(1):57–62
- Surhone LM, Timpelton MT, Marseken SF, Stokes GG (2010) *Stokes' law*. Betascript Publishing
- Tang Q, Hu J (2015a) Diversity of acoustic streaming in a rectangular acoustofluidic field. *Ultrasonics* 58:27–34
- Tang Q, Hu J (2015b) Analyses of acoustic streaming field in the probe-liquid-substrate system for nanotrapping. *Microfluid Nanofluid* 19(6):1395–1408
- Tang Q, Hu J, Qian S, Zhang X (2017a) Eckart acoustic streaming in a heptagonal chamber by multiple acoustic transducers. *Microfluid Nanofluid* 21:28
- Tang Q, Wang X, Hu J (2017b) Nano concentration by acoustically generated complex spiral vortex field. *Appl Phys Lett* 110(10):104105
- Vincent B, Destefanis V (2013) Method for fabricating a micro-electronic device equipped with semi-conductor zones on an insulator with a horizontal GE concentration gradient. US Patent, US 8,501,596 B2
- Wang H, Lu Y (2012) Morphological control of self-assembly polyaniline micro/nano-structures using dichloroacetic acid. *Synth Met* 162(15–16):1369–1374
- Yang B, Hu J (2014) Linear concentration of microscale samples under an ultrasonically vibrating needle in water on a substrate surface. *Sens Actuat B Chem* 193:472–477
- Zhou R, Wang P, Chang H (2006) Bacteria capture, concentration and detection by alternating current dielectrophoresis and self-assembly of dispersed single-wall carbon nanotubes. *Electrophoresis* 27(7):1376–1385
- Zhou Y, Hu J, Bhuyan S (2013) Manipulations of silver nanowires in a droplet on low-frequency ultrasonic stage. *IEEE Trans Ultrason Ferroelectr Freq Control* 60(3):622–629